Nucleation of Th-rich cerianite on halloysite surface in a regolith-hosted rare earth elements deposit in South China

Xiangjie Cui[†], Huan Liu[‡], Xiancai Lu[‡*], Juan Li[†], Jiani Chen[†], Ting-Shan Chan[§], Xiandong Liu[†], Rucheng Wang[†]

[†] State Key Laboratory for Mineral deposits Research, School of Earth Sciences and Engineering, Nanjing University, Nanjing, Jiangsu 210023, China

[‡] Key Laboratory of Surficial Geochemistry, Ministry of Education, School of Earth Sciences and Engineering, Nanjing University, Nanjing, Jiangsu 210023, China

[§]National Synchrotron Radiation Research Center, Hsinchu 30076, Taiwan

* Corresponding author: xcljun@nju.edu.cn (Xiancai Lu). Tel: +86-25-89681065

ABSTRACT

The ion-adsorption rare earth element (REE) deposit, a valuable type of REE deposit, has been thought being derived from the release and enrichment of REE during granite weathering. Understanding the REE occurrence in regolith-hosted deposits is crucial for more efficient extraction. We investigated a weathering granite profile of a regolith-hosted REE deposit located in South China. X-ray diffraction (XRD) and X-ray absorption near edge structure (XANES) analysis of the clay fractions reveal that the highest Ce(IV) content locates in intensely weathered layers, and cerianite nano-particles (CeNPs) can be observed besides invisible adsorbed REEs. Interestingly, most of the CeNPs scatter on halloysite basal surface and present obviously preferred orientation. Detailed analysis demonstrates that the diagonal plane of cerianite matches with the exposed basal surfaces (Si-O tetrahedron) of halloysite. Such a lattice match may contribute to the nucleation and growth of CeNPs after oxidation of the adsorbed Ce(III), which results in great REE enrichment by clays. The findings provide a new sight for understanding Ce precipitation and REE mineralization in granite weathering.

Key words: Nucleation; halloysite; lattice match; Cerianite; ion-adsorption rare earth element deposit; South China

INTRODUCTION

Rare earth elements (REEs) are not only critical metals widely used in developments of various functional materials, but also regarded as important geochemical indicators due to their unique properties (Chakhmouradian and Wall, 2012). Among the 14 REE members, Ce has attracted most attentions because of its high redox-sensibility. In natural settings, Ce commonly presents as less soluble tetravalent state (Ce(IV)) in oxidizing conditions and behaves differently from other REEs, which makes it enriched or depleted relatively to other REE members (Akagi and Masuda, 1998; Braun et al., 1990; Piepgras and Jacobsen, 1992). In general, Ce anomaly ($Ce/Ce^*=Ce_N/(La_N \times Pr_N)^{1/2}$) can be used to trace the redox conditions of sedimentary and diagenetic environments (Mukhopadhyay et al., 2014; Murakami et al., 2001). Its behaviors in weathering process reflect the geochemical cycle of REE including enrichment in specific layers and migration from parent rocks to rivers, groundwater and finally oceans (Leybourne and Johannesson, 2008; Singh, 2009; Su et al., 2017). Strong REE enrichment in specific layers of weathered granite profiles even leads to formation of ion-adsorption REE deposits, which have been widely discovered and exploited in South China (Li et al., 2017). Based on comprehensive investigation, three main occurrences of the REEs which were released from weathered primary REE-bearing minerals have been reported (Janots et al., 2015; Laveuf and Cornu, 2009; Li et al., 2017). Besides the dissolved REEs in pore water, part of the released REEs were adsorbed by clay and Fe-Mn oxides, which mainly present as the exchangeable states. The others, especially Ce(IV), precipitated as secondary minerals.

Among these various states of REEs, the formation of cerianite nano-particles (CeNP) represents the oxidation of Ce(III) and usually account for commonly observed Ce anomaly. Manganese oxides have been found playing important roles in Ce(III) oxidation and Ce(IV) precipitation in weathering processes (Janots et al., 2015; Santos et al., 2019). However, halloysite and kaolinite are the main components in regolith layers where cerianite particles on halloysite surface have been observed rather than any other minerals (Braun et al., 1990; Huang et al., 2021). However, little attention has been paid on the kinetic mechanism for crystallization of cerianite, especially, the selective growth on halloysite.

Halloysite, first described by Berthier (Berthier, 1826), is a dioctahedral 1:1 clay mineral of the kaolin group which differs from kaolinite in the intercalated water, widely observed in soils and weathered profiles (Joussein et al., 2005; Lu et al., 2016). In general, halloysite exhibits a tubular morphology due to the mismatch between tetrahedral and octahedral sheets (Singh, 1996). As the Si-O tetrahedral sheet is a little bigger than the Al-O octahedral sheet, the Si-O tetrahedral surface is always the external surface (Singh, 1996). Although halloysite and kaolinite generally act as the carrier of exchangeable REE and secondary cerianite particles (Bao and Zhao, 2008; Borst et al., 2020; Li and Zhou, 2020; Li et al., 2017), little attention has been focused on the effects of clay surfaces on REE precipitation behaviors. It has been reported that phyllosilicate or clay minerals can provide nucleation templates to induce heterogeneous nucleation and epitaxial growth of heavy metal phyllosilicate (Schlegel et al., 2001; Xu et al., 2018). In addition, surface

charge of clay minerals also facilitates heterogeneous precipitation (Fodor et al., 2020; Liu et al., 2019). However, the observed spatial relation between cerianite and halloysite was seldom discussed, and the contribution of halloysite to cerianite crystallization is still unclear.

In this study, we investigated a weathering profile of a REE-rich granite in South China where numerous ion-adsorption REE deposits have developed upon Mesozoic granite plutons (Bao and Zhao, 2008; He et al., 2017; Li et al., 2017), and secondary cerianite was found on halloysite surface. Multiple characterization techniques, including X-ray diffraction (XRD), high resolution transmission electron microscope (HR-TEM), scanning electron microscope (SEM) equipped with energy dispersive spectrometer (EDS), and X-ray absorption near edge structure (XANES), have been employed to reveal the relation between CeNP and underlying halloysite surface.

SAMPLES AND CHARACTERIZATION METHODS

We investigated a weathering granite profile with considerable REE enrichment at Gangxia in Anyuan County, Jiangxi Province, South China. The elemental geochemistry of this profile has been studied previously by our group (Liu et al., 2016). Four weathered layers upon the fresh granite, i.e., surface soil (0~0.5 m), alloterite layer (0.5~5 m), isalterite layer (5~10 m) and fissured layer (10~18 m) have been identified. The parent rock is a coarse-grained REE-rich biotite K-feldspar granite with accessory minerals such as magnetite, fluorite, zircon, apatite, and accessory REE minerals including bastnaesite, monazite, xenotime, and fergusonite. The granite is peraluminous (A/CNK (molar

$Al_2O_3/(CaO+Na_2O+K_2O))=1.18$) and enriches REEs (REE+Y=447 ppm, Ce/Ce*= 0.34) (Liu et al., 2016). The samples collected from the alloterite layer (REE+Y= 448 ppm, Ce/Ce*= 0.87) together with fresh granite samples were studied to reveal the effects of halloysite on cerianite crystallization. The shallow alloterite samples were not used because the high content of organic matters may affect Ce oxidation complicatedly (Davranche et al., 2005; Tanaka et al., 2010; Yu et al., 2018).

All alloterite samples were divided into two parts: one was pristine sample which was simply ground to 200 mesh in agate mortar, another was the clay fraction which was isolated via centrifugation according to the Stokes Law. The mineral composition of both the pristine samples and clay fractions have been determined based on XRD analysis on a Bruker d8 advance X-ray diffractometer. The pristine samples were loaded in XRD powder holders and made smooth surfaces with frosted-glass, and the clay fractions were prepared as oriented slides before analysis. XRD worked on a Cu target at 40 kV and 40 mA, with 2θ scanning range from 3° to 70° for powder samples and 3° to 36° for oriented slides, a step of 0.02° and dwell time of 0.3 s. Phase identification was performed using the JADE 9.5.1 with Materials Data Inc. The dispersion of clay fractions and pristine samples were dropped on amorphous carbon coated copper grids for SEM and HR-TEM observation. A Carl Zeiss Supra 55 SEM was used for search for REE minerals and morphology observation with 15 KeV and 5 KeV accelerating voltage respectively. A FEI Tecnai G2 F20 TEM was employed with an operated acceleration voltage of 200 KeV, and the equipped Oxford AZtec X-Max 80T EDS was used to detect their chemical

composition.

To determine the state of Ce in the samples, XANES spectra was collected at the beamline 16A1 (NSRRC, Taiwan) with an operating voltage at 1.5 GeV and a current of 360 mA. A double crystal Si (111) monochromator and a toroidal focusing mirror were used to focus the beam to 0.5×0.4 mm^2. Ce L3-edge (5723 eV) spectra were recorded in the fluorescence mode in an Ar gas chamber with a silicon drift detector (SDD). The energy steps and acquisition time were 4 eV-1 s, 1 eV-1.5 s, 0.2 eV-2 s and 0.06 eV-3 s in the 5573-5663, 5663-5713, 5713-5768 and 5768-5923 eV intervals, respectively. $CeCl_3$ and CeO_2 powders were taken as standards for Ce(III) and Ce(IV) analysis respectively. The spectra were analyzed by liner combination fitting (LCF) in Athena from IFEFFIT software package (Ravel and Newville, 2005).

RESULTS

The XRD patterns show that the primary minerals of granite include quartz, K-feldspar, plagioclase and biotite and the secondary minerals are mainly composed of halloysite (10 Å and 7 Å) and kaolinite (Figure 1). The wide peak at about 7.2 Å (2θ = 12.3^o) consists of the (001) diffraction peaks of both kaolinite and 7Å-halloysite, and 7Å-halloysite forms when 10Å-halloysite underwent irreversible dehydration (Yuan et al., 2015).

The Ce L3-edge XANES of fresh granite, weathered sample (WS) and its clay fraction (Figure 2) clearly indicate changes in Ce valence caused by weathering. The primary granite (Ce = 51 ppm) shows a low Ce(IV) proportion (Ce(IV)/Ce = 0.16),

however, the Ce(IV) proportion of weathered sample (Ce = 97 ppm) increases to 0.69, which indicates considerable oxidation of primary Ce(III) species. Furthermore, Ce(IV) proportion of the clay fractions increases to as high as 0.80, suggesting an enrichment of oxidized Ce in clay minerals. The Ce(III) left in the clay fraction may accommodate in tiny primary minerals as impurities.

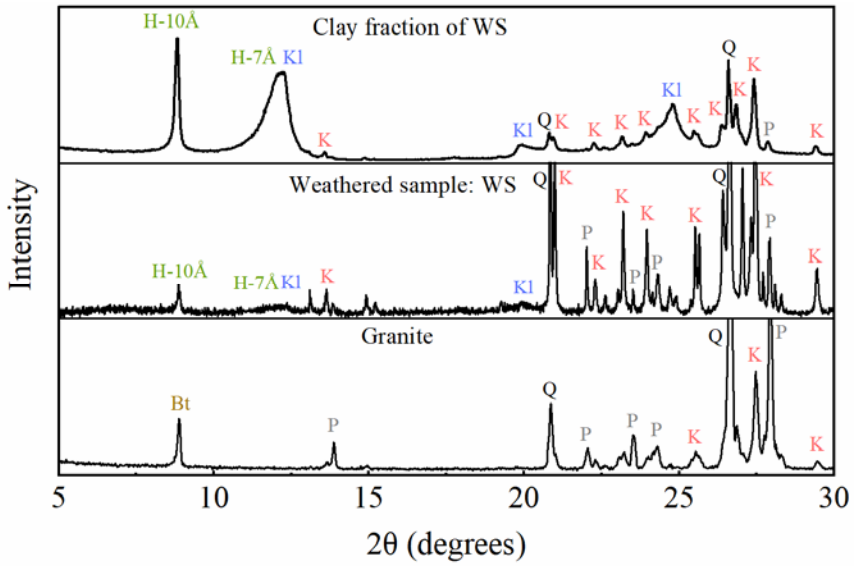

FIGURE 1. XRD patterns of fresh granite, weathered sample from alloterite layer (WS) and its clay fraction. H-10 Å: halloysite-10 Å; H-7 Å: halloysite-7 Å; Kl: kaolinite; Q: quartz; K: K-feldspar; P: plagioclase; Bt: biotite. For easy to distinguish, the XRD patterns only shows 5~30 deg, the whole XRD patterns are showed in supplementary information.

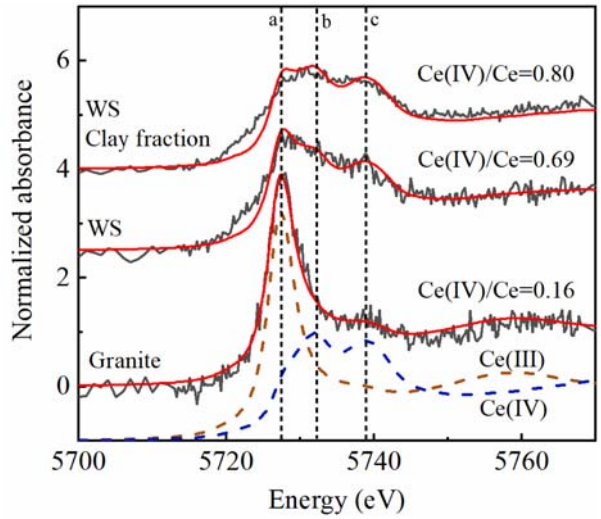

FIGURE 2. Ce L3-edge XANES spectra of fresh granite, weathered sample from the alloterite layer (WS) and its clay fraction. Black solid lines are experimental XANES data, red solid lines are fitting results, brown and blue dash lines are Ce(III) and Ce(IV) standards respectively. The Ce(III) spectrum shows a single peak (peak a) caused by the transition $2p_{3/2}\rightarrow(4f^{1})5d$, while the Ce(IV) spectrum shows Peak b and peak c attributed to $2p_{3/2}\rightarrow(4f^{1}\underline{L})5d$ and $2p_{3/2}\rightarrow(4f^{0})5d$ respectively (Takahashi et al., 2000). R factors are shown in supplementary information.

HR-TEM analysis reveals a common occurrence of secondary cerianite on tubular halloysite (Figure 3a, e and g) in the weathered samples (WS) collected from the alloterite layer. The halloysite generally presents as tubular particles with about 0.5~3.0 μm in length and 100~200 nm in diameter. Irregular aggregates of secondary cerianite nanoparticles with diameters of several nanometers can be observed on halloysite basal surfaces (Figure 3b). EDS analysis indicates that the CeNPs aggregates are enriched in

Th (average Ce molar ratio: Ce/(Ce+Th) = 0.84) (Figure 3a). There are obvious boundaries between CeNPs (blue dash lines in Figure 3b), however, the absence of diffraction rings in fast Fourier transform (FFT) analysis indicates a clear orientation of the aggregating CeNPs (Figure 3c). Three interplanar spacings are recognized as 3.1~3.2 Å in two directions and 2.80 Å, which well match to theoretical *d*(111)=3.12 Å, *d*(1-11) =3.12 Å and *d*(020)=2.71 Å of cerianite respectively (Figure 3b, c, f and h). These measured spacings are a little bigger than theoretical ones (Whitfield et al., 1966), which may be caused by the substitution of Th for Ce. Additionally, weak diffractions of *d*(-2-20) = 1.9 Å and *d*(-13-1) = 1.6 Å can be recognized in the FFT image (Figure 3g). Therefore, it can be concluded that (10-1) plane of CeNP directly contact to halloysite surface. Further, cerianite belongs to isometric crystal system and has an *Fm3m* space group, which means (10-1) plane has the same atomic arrangement with other diagonal planes and each of them can be the contact surface with halloysite. Top view of the diagonal plane is shown as Figure 3d, which shows the projection of cerianite unit cell in [10-1] direction and (111), (1-11) and (020) spacings.

This is the peer-reviewed, final accepted version for American Mineralogist, published by the Mineralogical Society of America.
The published version is subject to change. Cite as Authors (Year) Title. American Mineralogist, in press.
DOI: https://doi.org/10.2138/am-2022-8391. http://www.minsocam.org/

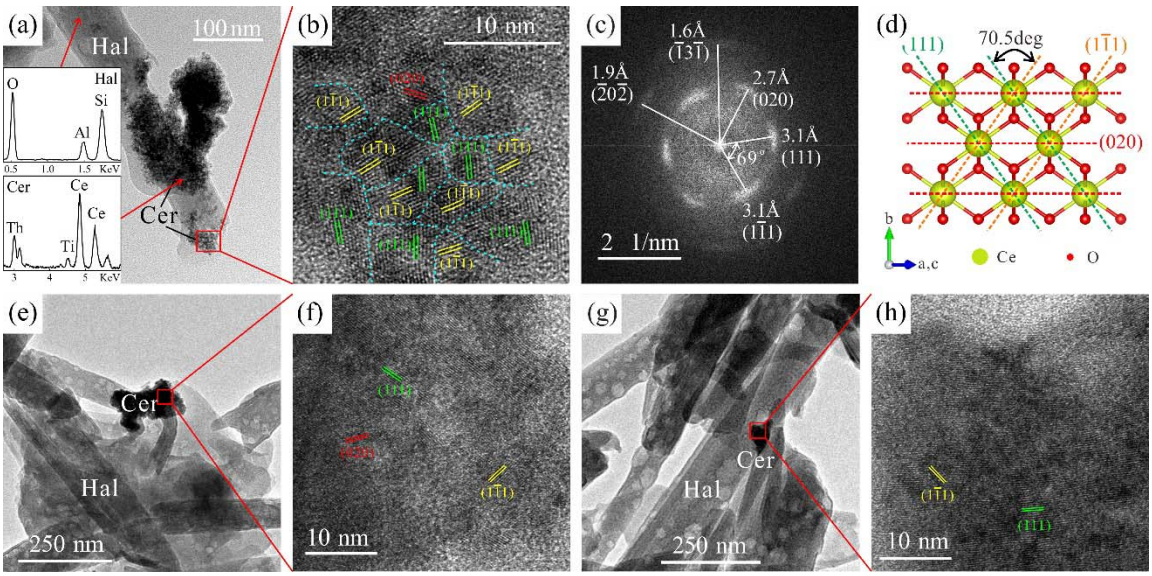

FIGURE 3. CeNP aggregates on tubular halloysite (a, e, and g) and their local enlarged images (b, f, and h); (c) FFT pattern of (b) showing (111), (1-11) and (020) planes of cerianite; (d): Cerianite unit cell from [10-1] direction. Hal: halloysite, Cer: cerianite.

DISCUSSION

The enrichment of REEs in the alloterite layer commonly results from continuous processes of decomposition of primary REE minerals, migration and chemical fixation of REEs involved by oxidation, adsorption and precipitation. In the weathering process of granite outcrops, most REEs were released from carrier minerals, such as bastnaesite. The released REEs were then adsorbed on to clay minerals with high specific surface area and abundant adsorption sites (Borst et al., 2020), and presented as exchangeable ions or precipitated as secondary REE minerals such as cerianite (Li et al., 2017). Recent studies reveal that Ce(IV) mainly enriched in Fe-Mn oxides in weathered profiles because Fe-Mn oxides can efficiently adsorb and oxidize Ce(III) (Ohnuki et al., 2015; Yu et al., 2017).

However, in the weathering profiles with very low content of Fe-Mn oxides, aggregates of CeNPs on halloysite surface, just like this study (Figure 3), can be observed (Huang et al., 2021). The observed CeNPs closely coexist with halloysite and attach on the basal surface near to the extremity of halloysite tubules, where no Fe-Mn oxide was detected via TEM-EDS or SEM-EDS (Figure 3a). Therefore, there should be other oxidants oxidizing Ce(III) and inducing formation of CeNPs. We think the atmospheric oxygen penetrated into weathering crust is the most possible oxidant. It has been also disclosed that dissolved O_2 in porewater or free oxygen in aeration zone may be the oxidant (Wheeler, 2016; Yu et al., 2006; Yu and O'Keefe, 2006). The oxidizing ability of oxygen was underestimated for a long time, because Ce usually coexists with Fe-Mn oxides in weathering profiles. Though the oxidation rate of Ce by dissolved O_2 is relatively low, the long term of weathering process could provide enough time to make this happen. In an experimental study, Ce(IV) precipitates were synthesized in O_2 gas bubbling condition after only 1 week (Nakada et al., 2013). Therefore, the CeNps on halloysite can be result from Ce oxidation by oxygen.

In this study, lots of CeNPs were observed on halloysite surface, indicating that the basal surface of halloysite played important roles in CeNPs precipitation. Many experimental and theoretical studies have revealed that clay surfaces can induce heterogeneous nucleation and growth on basal and edge surfaces (Dashtian et al., 2017; Ji et al., 2013; Liu et al., 2019; Schlegel et al., 2001; Xu et al., 2018; Zhang et al., 2019). In general, surface induced precipitation usually attributes to surface charge and/or lattice

match, which can provide nucleation sites and/or template. Previous studies have demonstrate that a preferred orientation in nucleation and growth of crystals is a consequence of lattice match between growth and template crystals, such as calcite on mica surface, Mn oxide on carbonate and MoS_2 on Mica (Heywood and Mann, 1994; Ji et al., 2013; Jun et al., 2005; Xu et al., 2018). As almost all the secondary CeNPs are orientationally aggregated, it is reasonable to deduce that the exposed (001) siloxane surface of halloysite can present as nucleation template of cerianite. The high lattice match between clay surface and growing mineral is considered as the important base and premise for formation of CeNPs because high match leads to lower structure strain and higher thermodynamic stability. For example, the clay edge surface has the same structure and similar lattice parameters with the metal-phyllosilicate, so a synchronous precipitation occurs with a small increase of free energy by only 1.7 kcal/mol (Zhang et al., 2019). In order to characterize the match between two contacting phases, we employ a parameter of lattice mismatch (f) as the follows:

$$\mathrm{f} = \frac{a_t - a_g}{a_t} \times 100\%$$

where a_t and a_g represent lattice parameters of the template crystal and the growth crystal respectively. Low mismatch f favors heterogeneous nucleation and growth, which has been proved by many typical mineral assemblages. Taking the muscovite-calcite system as an example, mismatches between corresponding calcite [001] plane and muscovite [001] plane are 4.3% and 6.8% in two directions, which can be corrected in the first few layers near the interface (Xu et al., 2018). As for halloysite-cerianite system in this study

(structures are showed in Figure 4), sizes of diagonal plane of cerianite are 7.65 Å and 5.41 Å in [01-1] and [100] directions respectively, while b = 9.164 Å and a = 5.02 Å in Si-O tetrahedral sheet(Frondel and Marvin, 1959; Singh, 1996). Mismatch between a direction of halloysite and [100] direction of cerianite is 7.8% which is acceptable, while mismatch between b direction of halloysite and [01-1] direction of cerianite is 16.5% which is relatively high. However, lattice parameters of halloysite are approximate, which present ideal Si-O hexagon surface without considering the layer curling and tetrahedral rotation in halloysite. The size of adjusted tetrahedral sheet are intermediate between the original tetrahedral sheet and the octahedral one, about a = 5.14 Å, b = 8.90 Å (Bates et al., 1950). On the other hand, lattice parameters of halloysite-related cerianite should be a little bigger than theoretical parameters due to the substitution of Th(IV) for Ce(IV) (a = 5.44 Å, b =7.69 Å) (Whitfield et al., 1966). Therefore, the mismatch between halloysite basal surface and cerianite diagonal plane is much less than 5.8% and 13.6% in two directions. In addition, sizes of cerianite nanoparticles are as small as about 10 nm and less, so the large lattice distortions of CeNPs together with the adjustable halloysite tubular surface can tolerate the mismatch between cerianite and halloysite. In short, the theoretical mismatch between halloysite (001) surfaces and cerianite diagonal planes could be greatly reduced via their lattice adjustments, such as Th-Ce substitution, surface structure relaxation, and template surface distortion. Similar adjustment of CeNP-kaolinite system is much limited, therefore no CeNP are observed on the surface of kaolinite surfaces.

Though adsorption capacity of edge surfaces of halloysite is commonly higher than that of basal surfaces, no CeNP observed on edge surfaces and tuber ends could be attributed to huge structural difference between cerianite and halloysite edge surface. On the (010) edge surface, which is usual end surface of tubular halloysite (Singh, 1996), the distance between two Al ions is 5.14 Å, and the distance of Al-O is 1.89 Å, while the Ce-Ce and Ce-O distances in cerianite are 3.85 Å and 2.35 Å, respectively. Accordingly, the mismatches in the two directions are 25.1% and 24.3%, which is greatly bigger than (001) surface. As for other residual minerals in weathering profiles, mismatches are also high. For quartz, Si-Si and Si-O distances are 3.06 Å and 1.61 Å respectively (Antao et al., 2008), and mismatches between cerianite and quartz are 25.8% and 46.0%. The mismatches between cerianite and feldspar are similar with mismatches between cerianite and quartz. Therefore, the basal surface of halloysite structurally favors cerianite nucleation more than edge surface and other residual minerals in weathering profiles.

As analysis above, CeNPs should exist on basal surface of halloysite tube randomly and even coat halloysite tube if Ce is sufficient, but CeNPs only exist near the end of halloysite tube and location with defects. We think such a phenomenon can be attributed to the pore water distribution in the top of weathering crusts. It is well known that pore water in sediments tends to hang from the downwards protruding position of pore walls during drying processes. When groundwater table falls in the weathering crusts, the infiltrated Ce(III)-bearing pore water preferred to accumulates at the end of halloysite tube and Ce(III) concentration gradually increased along evaporation processes.

Meanwhile, the penetrated atmospheric oxygen can oxidize the Ce(III) species into Ce(IV) and trigger the formation of secondary minerals. Therefore, Ce oxidation and precipitation mainly took place near to the end of halloysite tube. In addition, edge surfaces of halloysite tube don't support Ce precipitation because of larger lattice match, but can lead to Ce enrichment before precipitation by adsorption.

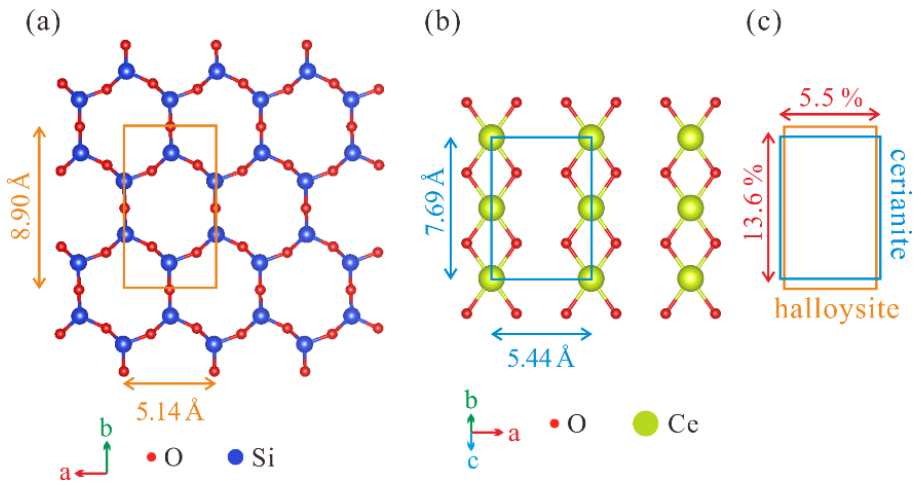

FIGURE 4. (a) (001) Surface of halloysite. (b) Diagonal plane of cerianite. (c) Comparison and lattice mismatch between (a) and (b).

Based on all abovementioned, we propose a model for secondary cerianite formation on halloysite surface (Figure 5). During the long-term weathering and repeated alternation of wetting and drying, primary Ce-bearing minerals, such as bastnaesite, biotite, apatite and so on, were gradually decomposed. Meanwhile, Ce was released into pore water and leached out from the upper part of the regolith profile to the groundwater table. In the processes, Ce(III) was oxidized into Ce(IV) possibly by free or dissolved oxygen in pore spaces. Ce ions tend to adsorb on halloysite surface, probably including

the edge surface due to its high reactivity, and cerianite preferred to nucleate on the basal surfaces, which provided templates and regulated orientationally aggregating of CeNPs.

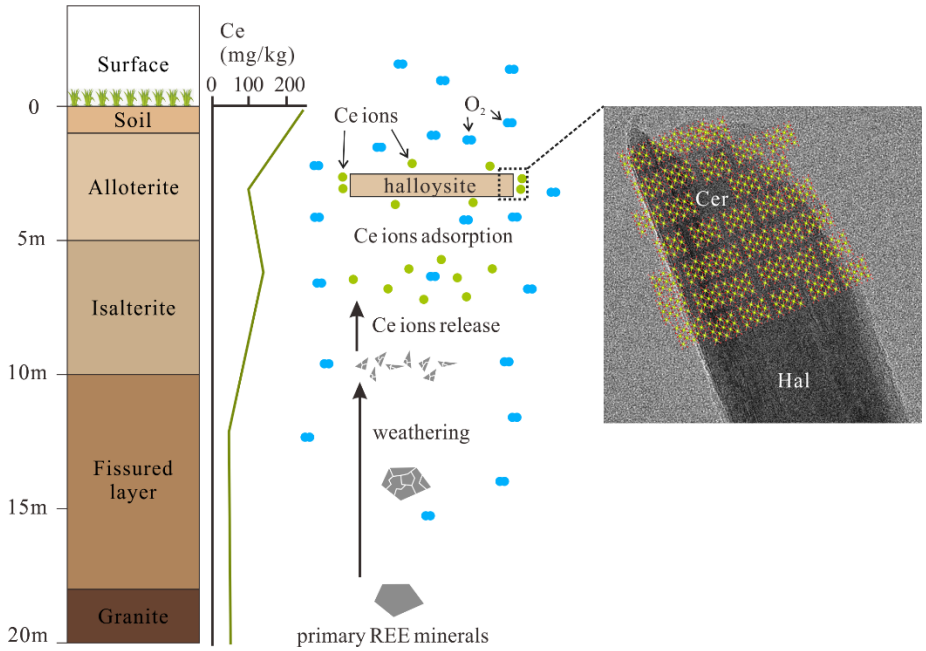

FIGURE 5. Schematic diagram of cerianite aggregate formation. (Cer: cerianite; Hal: halloysite)

IMPLICATION

The observed Ce precipitate in weathering profile is thought as the results of Ce mineral weathering, Ce(III) oxidation by oxygen, and CeNP nucleation on halloysite basal surface. This model reveals the effects of halloysite on nucleation and crystallization of cerianite, and provides new insights for understanding Ce enrichment in weathering process, especially in the weathering profiles where Fe-Mn oxides is scanty. The formation of CeNPs on halloysite inhibits Ce transportation to other REE accumulate layers, leading to the differentiation of among REE members in weathering processes

(Akagi and Masuda, 1998; Braun et al., 1990; Takahashi et al., 2000). However, synergistic effects of clay surfaces, Fe-Mn oxides and organic matters on Ce behavior need further studies.

The proposed model of CeNPs nucleation on halloysite surfaces related to lattice match can be adopted to understand the mineralization of other secondary minerals in surficial environment. Clay surfaces can act as excellent nucleation templates, because of good adsorption capacity and broad lattice matchability with other minerals such as carbonate, sulfide and halide (Ji et al., 2013; Pashley, 1956; Xu et al., 2018). In microscale, adsorption on surface leads to local enrichment of cations and then mineral nucleation happens when anions are introduced. Therefore, widespread clay minerals may be an important factor that controls precipitation of secondary minerals in natural environment including weathering profile, river and lake sediments.

Furthermore, clarifying the Ce occurrence is helpful for Ce extraction. In general, Ce is difficult to extract by traditional cationic leaching method, and reduction leaching via ascorbic acid or elemental sulfur have to be introduced to enhance the extraction efficiency (Xiao et al., 2017; Zhou et al., 2021). The formation of CeNPs in weathering profiles was controlled by halloysite and thus the effects of halloysite surface should be considered in technique development for enhancing Ce recovery.

ACKNOWLEDGEMENT: We acknowledge National Science Foundation of China (41730316, 41902032 and 41425009). H.L. is also supported by the Fundamental

Research Funds for the Central Universities (14380104). We are appreciated for the beamline of BL16A1 and BL01C1 in NSRRC for the XANES analysis.

REFERENCES

Akagi, T., and Masuda, A. (1998) A simple thermodynamic interpretation of Ce anomaly. Geochemical Journal, 32(5), 301-314.

Antao, S.M., Hassan, I., Wang, J., Lee, P.L., and Toby, B.H. (2008) State-of-the-art high-resolution powder x-ray diffraction (hrpxrd) illustrated with rietveld structure refinement of quartz, sodalite, tremolite, and meionite. The Canadian Mineralogist, 46(6), 1501-1509.

Bao, Z., and Zhao, Z. (2008) Geochemistry of mineralization with exchangeable REY in the weathering crusts of granitic rocks in South China. Ore Geology Reviews, 33(3-4), 519-535.

Bates, T.F., Hildebrand, F.A., and Swineford, A. (1950) Morphology and structure of endellite and halloysite. American Mineralogist, 35(7-8), 463-484.

Berthier, P. (1826) Analyse de l'halloysite. Ann. Chim. Phys., 32, 332-335.

Borst, A.M., Smith, M.P., Finch, A.A., Estrade, G., Villanova-de-Benavent, C., Nason, P., Marquis, E., Horsburgh, N.J., Goodenough, K.M., Xu, C., Kynicky, J., and Geraki, K. (2020) Adsorption of rare earth elements in regolith-hosted clay deposits. Nat Commun, 11(1), 4386.

Braun, J.J., Pagel, M., Muller, J.P., Bilong, P., Michard, A., and Guillet, B. (1990) Cerium anomalies in lateritic profiles. Geochimica Et Cosmochimica Acta, 54(3), 781-795.

Chakhmouradian, A.R., and Wall, F. (2012) Rare earth elements: Minerals, mines, magnets (and more). Elements, 8(5), 333-340.

Dashtian, H., Wang, H., and Sahimi, M. (2017) Nucleation of salt crystals in clay minerals:

Molecular dynamics simulation. J Phys Chem Lett, 8(14), 3166-3172.

Davranche, M., Pourret, O., Gruau, G., Dia, A., and Le Coz-Bouhnik, M. (2005) Adsorption of REE(III)-humate complexes onto MnO_2: Experimental evidence for cerium anomaly and lanthanide tetrad effect suppression. Geochimica et Cosmochimica Acta, 69(20), 4825-4835.

Fodor, M.A., Ható, Z., Kristóf, T., and Pósfai, M. (2020) The role of clay surfaces in the heterogeneous nucleation of calcite: Molecular dynamics simulations of cluster formation and attachment. Chemical Geology, 538.

Frondel, C., and Marvin, U.B. (1959) Cerianite, CeO_2, from pocos-de-caldas, brazil. American Mineralogist, 44(7-8), 882-884.

He, C., Xu, C., Zhao, Z., Kynicky, J., Song, W., and Wang, L. (2017) Petrogenesis and mineralization of REE-rich granites in Qingxi and Guanxi, Nanling region, South China. Ore Geology Reviews, 81, 309-325.

Heywood, B.R., and Mann, S. (1994) Template-directed nucleation and growth of inorganic materials. Advanced Materials, 6(1), 9-20.

Huang, J., He, H., Tan, W., Liang, X., Ma, L., Wang, Y., Qin, X., and Zhu, J. (2021) Groundwater controls REE mineralisation in the regolith of South China. Chemical Geology, 577.

Janots, E., Bernier, F., Brunet, F., Muñoz, M., Trcera, N., Berger, A., and Lanson, M. (2015) Ce(III) and Ce(IV) (re)distribution and fractionation in a laterite profile from Madagascar: Insights from in situ XANES spectroscopy at the Ce LIII-edge. Geochimica et Cosmochimica Acta, 153, 134-148.

Ji, Q., Zhang, Y., Gao, T., Zhang, Y., Ma, D., Liu, M., Chen, Y., Qiao, X., Tan, P.H., Kan, M., Feng, J., Sun, Q., and Liu, Z. (2013) Epitaxial monolayer MoS_2 on mica with novel photoluminescence. Nano Lett, 13(8), 3870-3877.

Joussein, E., Petit, S., Churchman, J., Theng, B., Righi, D., and Delvaux, B. (2005) Halloysite clay minerals - A review. Clay Minerals, 40(4), 383-426.

Jun, Y.S., Kendall, T.A., Martin, S.T., Friend, C.M., and Vlassak, J.J. (2005) Heteroepitaxial

nucleation and oriented growth of manganese oxide islands on carbonate minerals under aqueous conditions. Environmental Science & Technology, 39(5), 1239-1249.

Laveuf, C., and Cornu, S. (2009) A review on the potentiality of rare earth elements to trace pedogenetic processes. Geoderma, 154(1-2), 1-12.

Leybourne, M.I., and Johannesson, K.H. (2008) Rare earth elements (REE) and yttrium in stream waters, stream sediments, and Fe–Mn oxyhydroxides: Fractionation, speciation, and controls over REE+Y patterns in the surface environment. Geochimica et Cosmochimica Acta, 72(24), 5962-5983.

Li, M.Y.H., and Zhou, M.-F. (2020) The role of clay minerals in formation of the regolith-hosted heavy rare earth element deposits. American Mineralogist, 105(1), 92-108.

Li, Y.H.M., Zhao, W.W., and Zhou, M.-F. (2017) Nature of parent rocks, mineralization styles and ore genesis of regolith-hosted REE deposits in South China: An integrated genetic model. Journal of Asian Earth Sciences, 148, 65-95.

Liu, D., Xu, Y., Papineau, D., Yu, N., Fan, Q., Qiu, X., and Wang, H. (2019) Experimental evidence for abiotic formation of low-temperature proto-dolomite facilitated by clay minerals. Geochimica et Cosmochimica Acta, 247, 83-95.

Liu, R., Wang, R., Lu, X., and Li, J. (2016) Nano-sized rare earth minerals from granite-related weathering-type REE deposites in southern Jiangxi. Acta Petrologica Et Mineralogica, 35(4), 617-626.

Lu, Y., Wang, R., Lu, X., Li, J., and Wang, T. (2016) Reprint of genesis of halloysite from the weathering of muscovite: Insights from microscopic observations of a weathered granite in the Gaoling area, Jingdezhen, China. Applied Clay Science, 119, 59-66.

Mukhopadhyay, J., Crowley, Q.G., Ghosh, S., Ghosh, G., Chakrabarti, K., Misra, B., Heron, K., and Bose, S. (2014) Oxygenation of the Archean atmosphere: New paleosol constraints from eastern India. Geology, 42(10), 923-926.

Murakami, T., Utsunomiya, S., Imazu, Y., and Prasad, N. (2001) Direct evidence of late Archean to early Proterozoic anoxic atmosphere from a product of 2.5 Ga old weathering. Earth

and Planetary Science Letters, 184(2), 523-528.

Nakada, R., Takahashi, Y., and Tanimizu, M. (2013) Isotopic and speciation study on cerium during its solid–water distribution with implication for Ce stable isotope as a paleo-redox proxy. Geochimica et Cosmochimica Acta, 103, 49-62.

Ohnuki, T., Jiang, M., Sakamoto, F., Kozai, N., Yamasaki, S., Yu, Q., Tanaka, K., Utsunomiya, S., Xia, X., Yang, K., and He, J. (2015) Sorption of trivalent cerium by a mixture of microbial cells and manganese oxides: Effect of microbial cells on the oxidation of trivalent cerium. Geochimica et Cosmochimica Acta, 163, 1-13.

Pashley, D.W. (1956) The study of epitaxy in thin surface films. Advances in Physics, 5(18), 173-240.

Piepgras, D.J., and Jacobsen, S.B. (1992) The behavior of rare-earth elements in seawater - precise determination of variations in the north pacific water column. Geochimica Et Cosmochimica Acta, 56(5), 1851-1862.

Ravel, B., and Newville, M. (2005) ATHENA, ARTEMIS, HEPHAESTUS: data analysis for X-ray absorption spectroscopy using IFEFFIT. Journal of Synchrotron Radiation, 12, 537-541.

Santos, J.C.B.d., Le Pera, E., Oliveira, C.S.d., Souza Júnior, V.S.d., Pedron, F.d.A., Corrêa, M.M., and Azevedo, A.C.d. (2019) Impact of weathering on REE distribution in soil-saprolite profiles developed on orthogneisses in Borborema Province, NE Brazil. Geoderma, 347, 103-117.

Schlegel, M.L., Manceau, A., Charlet, L., Chateigner, D., and Hazemann, J.L. (2001) Sorption of metal ions on clay minerals. III. Nucleation and epitaxial growth of Zn phyllosilicate on the edge of hectorite. Geochimica Et Cosmochimica Acta, 65(22), 4155-4170.

Singh, B. (1996) Why does halloysite roll? - A new model. Clays and Clay Minerals, 44(2), 191-196.

Singh, P. (2009) Major, trace and REE geochemistry of the Ganga River sediments: Influence of provenance and sedimentary processes. Chemical Geology, 266(3-4), 242-255.

Su, N., Yang, S., Guo, Y., Yue, W., Wang, X., Yin, P., and Huang, X. (2017) Revisit of rare earth element fractionation during chemical weathering and river sediment transport. Geochemistry, Geophysics, Geosystems, 18(3), 935-955.

Takahashi, Y., Shimizu, H., Kagi, H., Yoshida, H., Usui, A., and Nomura, M. (2000) A new method for the determination of Ce-III/Ce-IV ratios in geological materials; application for weathering, sedimentary and diagenetic processes. Earth and Planetary Science Letters, 182(3-4), 201-207.

Tanaka, K., Tani, Y., Takahashi, Y., Tanimizu, M., Suzuki, Y., Kozai, N., and Ohnuki, T. (2010) A specific Ce oxidation process during sorption of rare earth elements on biogenic Mn oxide produced by Acremonium sp. strain KR21-2. Geochimica et Cosmochimica Acta, 74(19), 5463-5477.

Wheeler, D.W. (2016) Kinetics and mechanism of the oxidation of cerium in air at ambient temperature. Corrosion Science, 111, 52-60.

Whitfield, H.J., Roman, D., and Palmer, A.R. (1966) X-ray study of the system ThO_2-CeO_2-Ce_2O_3. Journal of Inorganic and Nuclear Chemistry, 28(12), 2817-2825.

Xiao, Y., Lai, F., Huang, L., Feng, Z., and Long, Z. (2017) Reduction leaching of rare earth from ion-adsorption type rare earths ore: II. Compound leaching. Hydrometallurgy, 173, 1-8.

Xu, H., Zhou, M., Fang, Y., and Teng, H.H. (2018) Effect of mica and hematite (001) surfaces on the precipitation of calcite. Minerals, 8(1), 17.

Yu, C., Boily, J.-F., Shchukarev, A., Drake, H., Song, Z., Hogmalm, K.J., and Åström, M.E. (2018) A cryogenic XPS study of Ce fixation on nanosized manganite and vernadite: Interfacial reactions and effects of fulvic acid complexation. Chemical Geology, 483, 304-311.

Yu, C., Drake, H., Mathurin, F.A., and Åström, M.E. (2017) Cerium sequestration and accumulation in fractured crystalline bedrock: The role of Mn-Fe (hydr-)oxides and clay minerals. Geochimica et Cosmochimica Acta, 199, 370-389.

Yu, P., Hayes, S.A., O'Keefe, T.J., O'Keefe, M.J., and Stoffer, J.O. (2006) The phase stability of cerium species in aqueous systems. Journal of The Electrochemical Society, 153(1),

C74-C79.

Yu, P., and O'Keefe, T.J. (2006) The phase stability of cerium species in aqueous systems. Journal of The Electrochemical Society, 153(1), C80-C85.

Yuan, P., Tan, D., and Annabi-Bergaya, F. (2015) Properties and applications of halloysite nanotubes: Recent research advances and future prospects. Applied Clay Science, 112, 75-93.

Zhang, C., Liu, X., Lu, X., Meijer, E.J., and Wang, R. (2019) Understanding the heterogeneous nucleation of heavy metal phyllosilicates on clay edges with first-principles molecular dynamics. Environ Sci Technol, 53(23), 13704-13712.

Zhou, F., Xiao, Y., Guo, M., Tang, Y., Zhang, W., and Qiu, R. (2021) Selective leaching of rare earth elements from ion-adsorption rare earth tailings: A synergy between CeO_2 reduction and Fe/Mn stabilization. Environ Sci Technol, 55, 11328-11337.